

Relationship between Duplex Grain Structure and Grain-boundary Precipitates in Ni₂M-stabilized Alloy

Toshiaki HORIUCHI^{1,*} and Naohiro SATOH¹

¹ Hokkaido Institute of Technology, 7-15-4-1, Maeda, Teine-ku, Sapporo, Hokkaido 006-8585, Japan

ABSTRACT

An experimental characterization of grain boundaries using field-emission Auger electron spectroscopy has been carried out for Ni₂M-stabilized alloy (where M mainly corresponds to Cr) and Alloy 690, which have duplex and non-duplex grain sizes, respectively, in order to determine the relationship between grain-boundary precipitates and the grain structure. Thermodynamic calculations based on the Scheil-Gulliver model with and without back diffusion of the C solute in the solid phase were also performed in order to investigate the solidification process in both alloys. Chromium carbide precipitates, with a predicted composition of M₂₃C₆, were observed at grain boundaries in both the Ni₂M-stabilized alloy and Alloy 690. The M₂₃C₆ precipitates in the Ni₂M-stabilized alloy were considerably coarser than those in the Alloy 690. A small number of coarse titanium carbonitride precipitates were also observed on the fracture surfaces of both alloys at intergranular and intragranular positions. The simulations predicted that the M₂₃C₆ precipitates are likely to be formed during the final stages of solidification, and it is thought that this occurs more readily in the Ni₂M-stabilized alloy. The results indicate that the duplex grain structure observed in the Ni₂M-stabilized alloy is most likely due to the presence of undissolved coarse M₂₃C₆ grain-boundary precipitates.

KEYWORDS

Ni₂M-stabilized alloy, Alloy 690, bimodal grain size distribution, M₂₃C₆ carbide, Scheil-Gulliver model, phase stability, thermodynamic calculation, Thermo-Calc, stress corrosion cracking

ARTICLE INFORMATION

Article history:
Received 30 June 2013
Accepted 2 October 2013

1. Introduction

A duplex grain structure is one in which both relatively coarse and fine grains are present, and has been investigated for over half a century. In 1957, Masuko reported the effect of a duplex austenite grain structure on the mechanical properties of steel, and categorized the grain size distribution as either “uniform” or “non-uniform” in which fine grains disperse homogeneously or locally (it sometimes shows a banded microstructure), respectively [1,2]. He pointed out that the strength and ductility of steel were strongly influenced by the grain size distribution. In particular, steel with a non-uniform duplex grain structure was found to exhibit lower strength and ductility than other types of steel. He also showed that a non-uniform duplex grain structure was formed as a result of primary segregation of grain-growth inhibitors, and that it also occurred in hyper-eutectoid steel due to primary segregation of carbides [3,4].

Duplex grain structures are sometimes observed in Ni-base superalloys, which are often used as structural materials in nuclear power plants. Mills *et al.* reported that Alloy 600 plate exhibited such a duplex grain structure, containing both fine grains with a mean diameter of ~20μm and coarse grains with a mean diameter of ~120μm, together with intergranular and intragranular M₇C₃ carbides and MC-type inclusions [5]. Hyatt *et al.* reported that a banded duplex grain structure with segregated carbide regions was found in electron beam welded Alloy 625 plate [6]. Shen summarized recent studies on the effect of cold working on stress corrosion cracking (SCC) in Alloy 690 [7]. He reported that a duplex grain structure was found in some Alloy 690 plates, in which the larger and smaller grains formed clear bands with linear streaks of TiN inclusions along the bands of smaller grains. These Alloy 690 plates with a duplex grain structure were found to exhibit higher crack growth rates, whether the banded microstructure was present or not [8,9]. Shen also reported that there was no clear

*Corresponding author, E-mail: horiuchi@hit.ac.jp

relationship between the inhomogeneous microstructure due to banding and crack growth rates, and that the presence of such banding did not guarantee higher crack growth rates. Alloy 690 was introduced as a replacement material for Alloy 600, and SCC in Alloy 690 has not yet been observed except in accelerated laboratory tests. However, from the above discussion, it is clear that many uncertainties remain with regard to the formation and characteristics of duplex grain structures in Alloy 690. From the viewpoint of proactive materials degradation management, it is therefore essential to form a fuller understanding of the duplex grain structure in Alloy 690, especially with regard to grain boundaries.

The authors have recently developed a Ni₂M-stabilized alloy by deliberately removing Fe from standard Alloy 690 in order to promote long-range ordering of intermetallic Ni₂M (where M mainly corresponds to Cr) [10,11]. This was performed for the purpose of investigating the influence of such ordering on SCC, which will be carried out in the near future. A duplex grain structure was found only in the Ni₂M-stabilized alloy, and not in the original Alloy 690. In the present study, the grain structure in both alloys was experimentally investigated with a particular focus on grain-boundary precipitates. Thermodynamic calculations based on the Scheil-Gulliver model [12,13] were also carried out in order to determine the solidification process for the alloys.

2. Experimental and Calculation Procedure

2.1. Experimental Procedure

The chemical compositions of the Ni₂M-stabilized alloy and Alloy 690 used in the present study are shown in Table 1 [10]. The Fe content in the Ni₂M-stabilized alloy is extremely low, which places it beyond the specifications for Alloy 690 [14]. Although the Cu content is relatively high, it is still within the Alloy 690 specifications. The Alloy 690 was melted in a commercial size, while the 17 kg of the Ni₂M-stabilized alloy was laboratory melted in a vacuum induction furnace. They were subsequently hot forged and hot rolled. Simulated mill annealing (MA) was then carried out for 45 min at 1050°C for the Ni₂M-stabilized alloy and at 1075°C for the Alloy 690, followed by quenching in water. Subsequently, both alloys were subjected to a thermal treatment (TT) at 700°C for 15 h, followed by cooling in air. Test specimens were cut and polished, and were electrolytically polished using a potentiostat in an aqueous solution of phosphoric acid. Microstructural observations were carried out using an optical microscope, and Vickers hardness measurements were performed with an indentation load of 98 N. In addition, cylindrical specimens with a gauge diameter of 1.0 mm and a gauge length of 4.7 mm were cut for grain-boundary analysis. The specimens were electrolytically polished to remove surface alteration layers formed during the machining process, and were then subjected to electrolyzation in an aqueous solution of sulfuric acid and thiourea at a current density of 5 mA/cm² for up to 500 h for hydrogen charging. They were then ruptured under a constant strain rate of 5.0×10⁻⁷ /s in a high vacuum of less than 10⁻⁷ Pa. Finally, the fracture surfaces of the specimens were characterized by field-emission Auger electron spectroscopy (FE-AES; ULVAC-PHI PHI 680) when still connected to the constant-strain-rate testing device under a high vacuum.

2.2. Calculation Procedure

The following conditions are assumed in the Scheil-Gulliver model [12,13]: (1) no diffusion occurs in the formed solid, (2) instantaneous diffusion occurs in the liquid, (3) phase equilibrium

Table 1 Chemical compositions of Ni₂M-stabilized alloy and Alloy 690 (wt%) [10]

	C	Si	Mn	Cr	Fe	Cu	Ti	Ni
Ni ₂ M-stabilized alloy	0.020	0.3	0.3	29	0.1	0.4	0.24	bal.
Alloy 690	0.019	0.3	0.3	30	9.4	0.04	0.23	bal.

exists at the solid-liquid interface and (4) the solidus and liquidus lines are straight segments. Further details about the model are beyond the scope of the present study, and are available in the literature [15,16]. Thermodynamic calculations for the solidification process were performed using the Thermo-Calc software package (Ver. S) [17] with the Ni-DATA (Ver. 8) thermodynamic database by ThermoTech [18]. The chemical compositions used were those listed in Table 1, and a pressure of 10^5 Pa was assumed. Calculations were also performed in which the effect of back diffusion of the C solute in the solid phase was considered. Thermodynamic phase equilibrium calculations were carried out based on the calculated chemical compositions of the liquid phase during the final stages of solidification in order to investigate any differences between the solidification process for the Ni₂M-stabilized alloy and Alloy 690.

3. Results and Discussion

3.1. Experimental Results and Discussion

Figure 1 presents optical micrographs of the Ni₂M-stabilized alloy and Alloy 690 following the TT process. The measured Vickers hardness is also indicated. Although there is no significant difference in Vickers hardness between the alloys, the Ni₂M-stabilized alloy exhibits a somewhat banded microstructure with a duplex grain size; similar results were obtained following the MA process [10].

FE-AES secondary electron images (SEIs) of the fracture surface of the Ni₂M-stabilized alloy after constant-strain-rate testing are shown in Fig. 2; it can be seen that some of the fracture is intergranular. Similar results were obtained for the Alloy 690 sample. Figure 3 and 4 show SEIs and elemental maps for Ni, Cr, C, P, Fe, Ti and B at grain boundaries of smaller grains in the Ni₂M-stabilized alloy and Alloy 690, respectively. In each map, the intensity indicates the concentration of that particular element. It should be noted that for both alloys, the Cr and C are concentrated in regions associated with particles or surface asperities in the corresponding SEI. The results of FE-AES spot analyses indicated that these regions are chromium carbide precipitates, with a predicted composition of M₂₃C₆ based on previous thermodynamic equilibrium calculations [11]. As can be clearly seen, the coarse precipitates with a diameter of *ca.* 1 μ m are found only in the Ni₂M-stabilized alloy. Since it seems quite unlikely that such coarse precipitates were formed during the TT or MA process, it is reasonable to assume that they were formed during the solidification process.

As shown in Figs. 3 and 4, although P shows a tendency to segregate at grain boundaries, Fe, Ti and B do not. In fact, for both alloys, only a few coarse titanium carbonitride precipitates are observed on either intergranular or intragranular fracture surfaces. Moreover, based on a FE-AES analysis of the intragranular fracture surfaces, no localization of any of the analyzed elements occurs inside grains. Thus, it can be concluded that the main microstructural difference between the Ni₂M-stabilized alloy and the Alloy 690 is the presence of coarser chromium carbide precipitates at the grain boundaries of the Ni₂M-stabilized alloy. This may have a significant influence on the formation of the duplex grain structure in this alloy. The coarse chromium carbide precipitates will be discussed in the next section in terms of the solidification process for both alloys.

3.2. Calculation Results and Discussion

The results of thermodynamic equilibrium calculations carried out in our previous study [11] indicate that M₂₃C₆ would precipitate at around 1000°C in both the Ni₂M-stabilized alloy and the Alloy 690. Figure 5 shows the calculation results for the solidification process for the two alloys using the Scheil-Gulliver model. Here, “fcc” indicates a matrix with a face-centered cubic crystal structure. The results indicate that for both alloys, almost all of the M₂₃C₆ is crystallized directly from the liquid during the final stages of solidification, rather than being formed by precipitate growth in the solid phase.

Table 2 lists the calculated chemical compositions of the liquid phase during the final stages of solidification for both alloys, and Fig. 6 shows the calculated phase equilibrium diagrams using these compositions. It can be seen that crystallization of M₂₃C₆ is expected to occur from the liquid. The

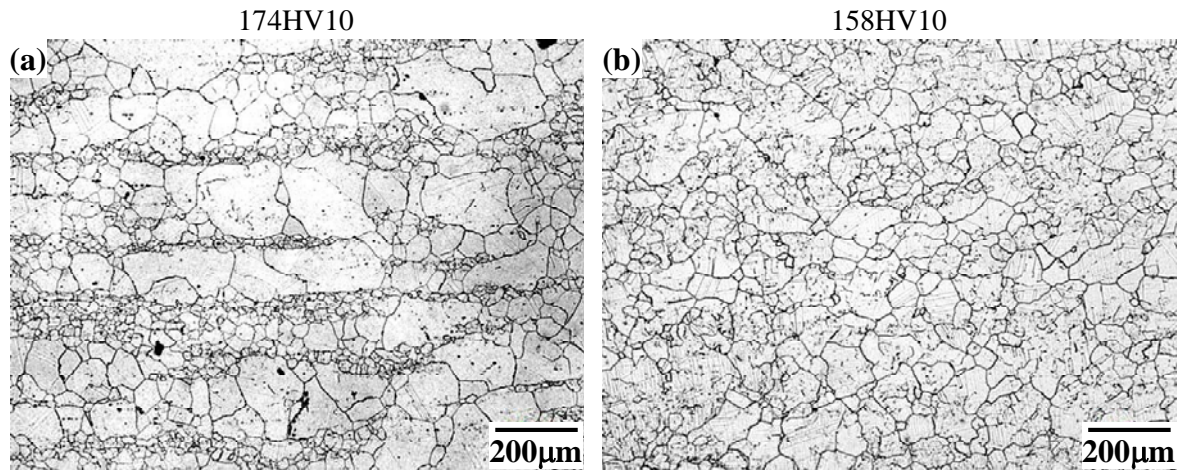


Fig. 1 Optical micrographs of (a) Ni₂M-stabilized alloy and (b) Alloy 690 following TT process [10]. The Vickers hardness for each alloy is indicated.

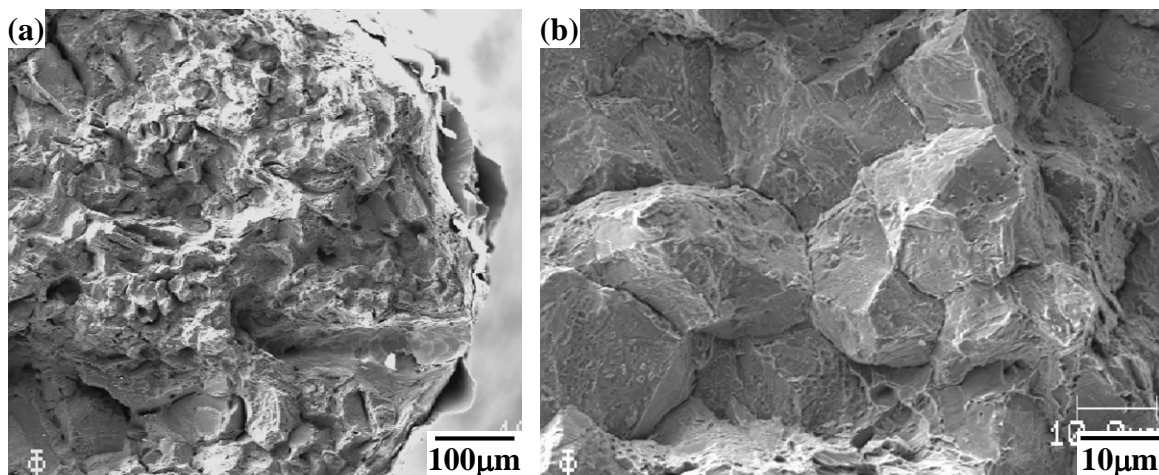


Fig. 2 SEIs of fracture surface of Ni₂M-stabilized alloy following TT process. Image (b) is a magnified version of (a).

mole fractions of M₂₃C₆ at the end of the solidification process are about 11% and 7% for the Ni₂M-stabilized alloy and the Alloy 690, respectively, implying that it forms more easily in the Ni₂M-stabilized alloy. The essential difference between the two phase equilibrium diagrams in Fig. 6 is that TiC is expected to crystallize from the liquid only in the Alloy 690. This may be because the solubility of titanium in the Alloy 690 matrix is lower than that in the Ni₂M-stabilized alloy matrix, which results in a higher titanium concentration in the liquid phase for the Alloy 690, as shown in Table 2, thus enhancing the stability of TiC.

Figure 7 shows the calculation results for the solidification process for the two alloys using the Scheil-Gulliver model with back diffusion of the C solute in the solid phase taken into consideration. The results indicate that only the matrix is expected to be solidified, with no M₂₃C₆ formation during the solidification process for either alloy. The chemical compositions of the liquid phase during the final stages of solidification are shown in Table 3, and the calculated phase equilibrium diagrams based on these compositions are shown in Fig. 8. Formation of M₂₃C₆ is expected only for the Ni₂M-stabilized alloy, which implies that M₂₃C₆ carbide is more likely to form in the Ni₂M-stabilized alloy during the solidification process. In addition, a relatively large amount of TiC is expected to form in the Alloy 690 compared to the Ni₂M-stabilized alloy. This is again thought to be due to the lower solubility of titanium in the Alloy 690 matrix, as discussed earlier.

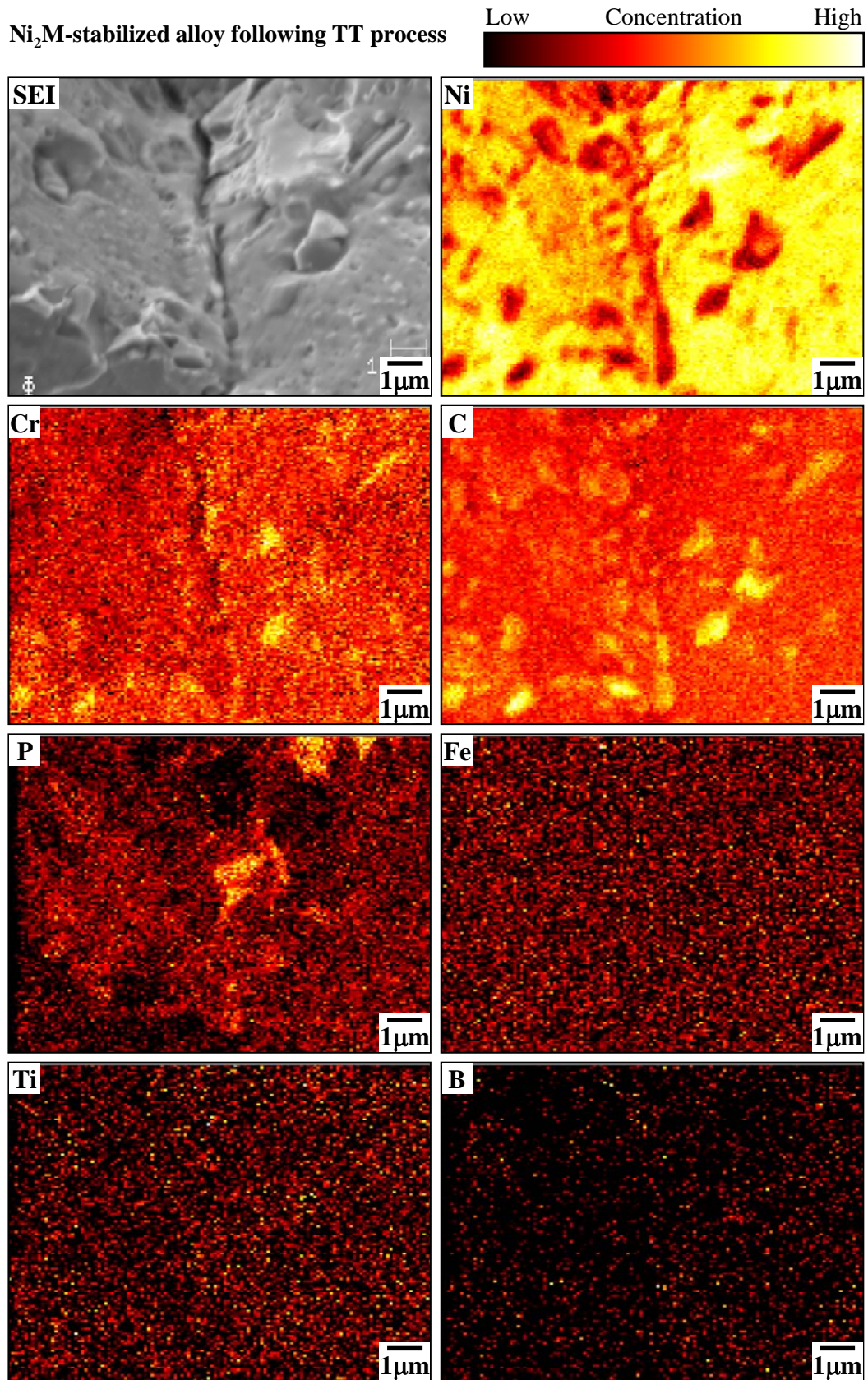


Fig. 3 SEI and elemental maps by FE-AES for Ni, Cr, C, P, Fe, Ti and B at grain boundaries of smaller grains in Ni₂M-stabilized alloy following TT process.

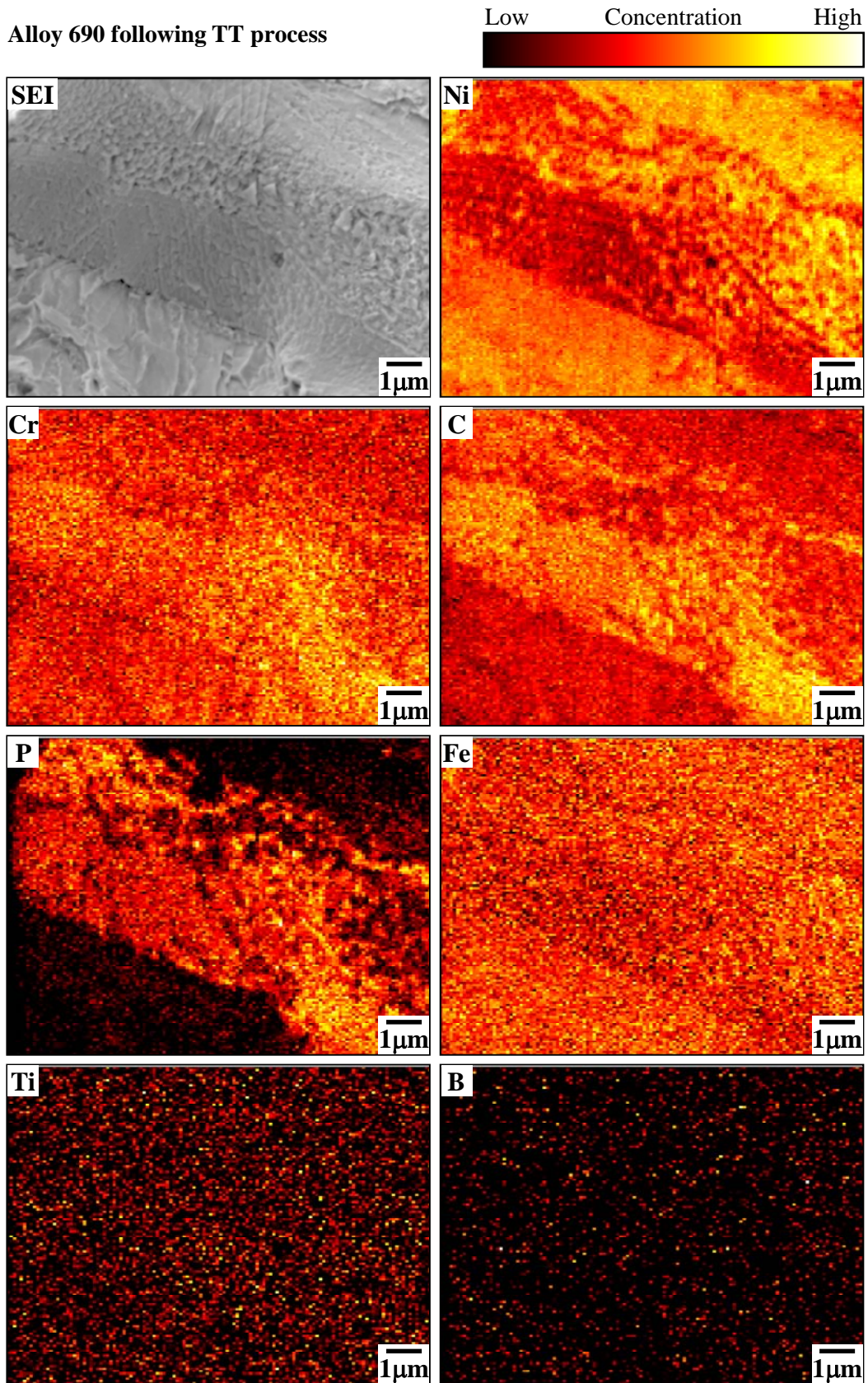


Fig. 4 SEI and elemental maps by FE-AES for Ni, Cr, C, P, Fe, Ti and B at grain boundaries in Alloy 690 following TT process.

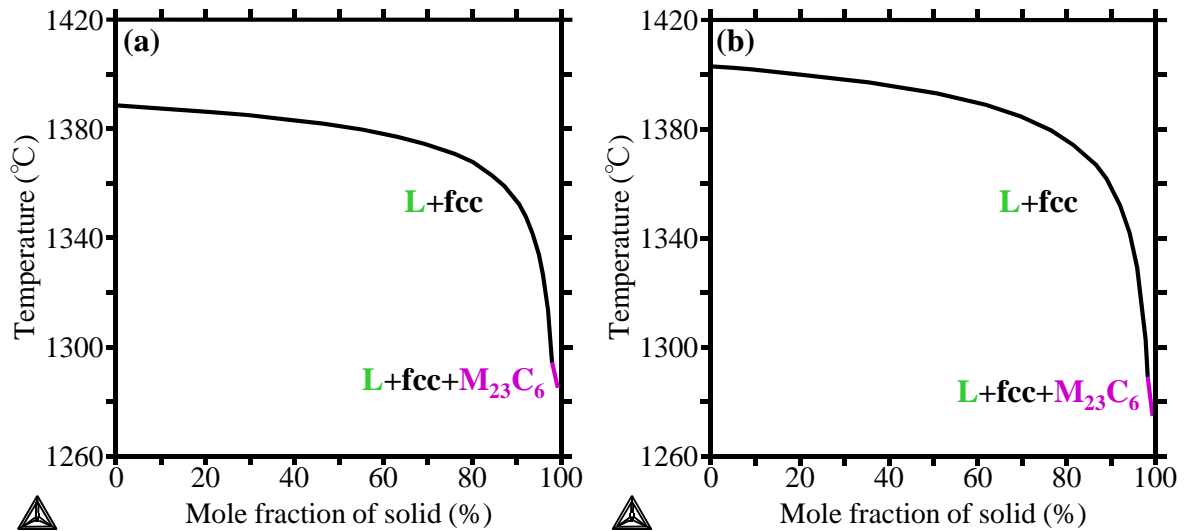


Fig. 5 Calculated solidification results based on Scheil-Gulliver model for (a) Ni_2M -stabilized alloy and (b) Alloy 690.

Table 2 Calculated chemical compositions (wt%) of liquid phase during final stages of solidification based on Scheil-Gulliver model

	C	Si	Mn	Cr	Fe	Cu	Ti	Ni
Ni_2M -stabilized alloy	0.59	0.6	1.7	37	0.05	2.3	1.5	bal.
Alloy 690	0.58	0.8	1.5	40	5.1	0.2	2.0	bal.

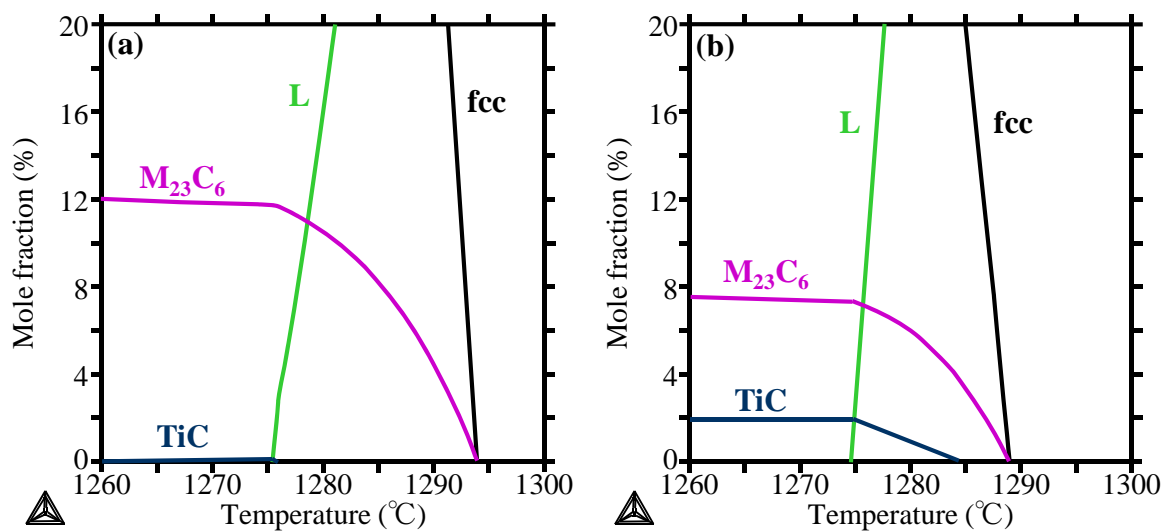


Fig. 6 Calculated phase equilibrium diagrams based on chemical compositions of liquid phase during final stages of solidification shown in Table 2 for (a) Ni_2M -stabilized alloy and (b) Alloy 690.

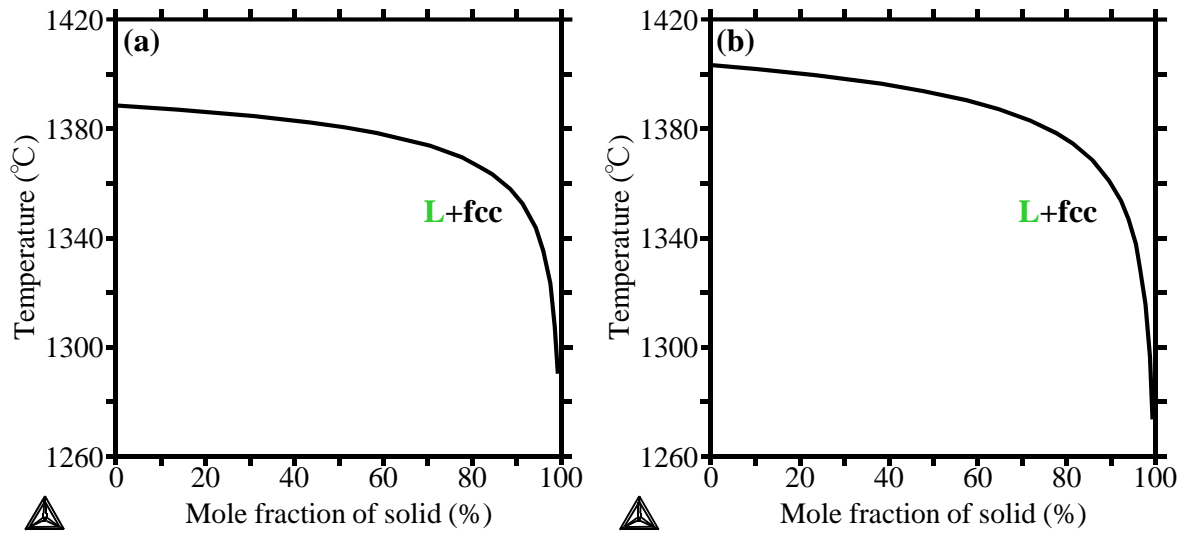


Fig. 7 Calculated solidification results based on Scheil-Gulliver model with back diffusion of C solute in solid phase taken into consideration for (a) Ni₂M-stabilized alloy and (b) Alloy 690.

Table 3 Calculated chemical compositions (wt%) of liquid phase during final stages of solidification based on Scheil-Gulliver model with back diffusion of C solute in solid phase taken into consideration

	C	Si	Mn	Cr	Fe	Cu	Ti	Ni
Ni ₂ M-stabilized alloy	0.20	0.9	2.4	35	0.04	2.3	2.2	bal.
Alloy 690	0.27	1.1	2.1	39	4.3	0.2	3.2	bal.

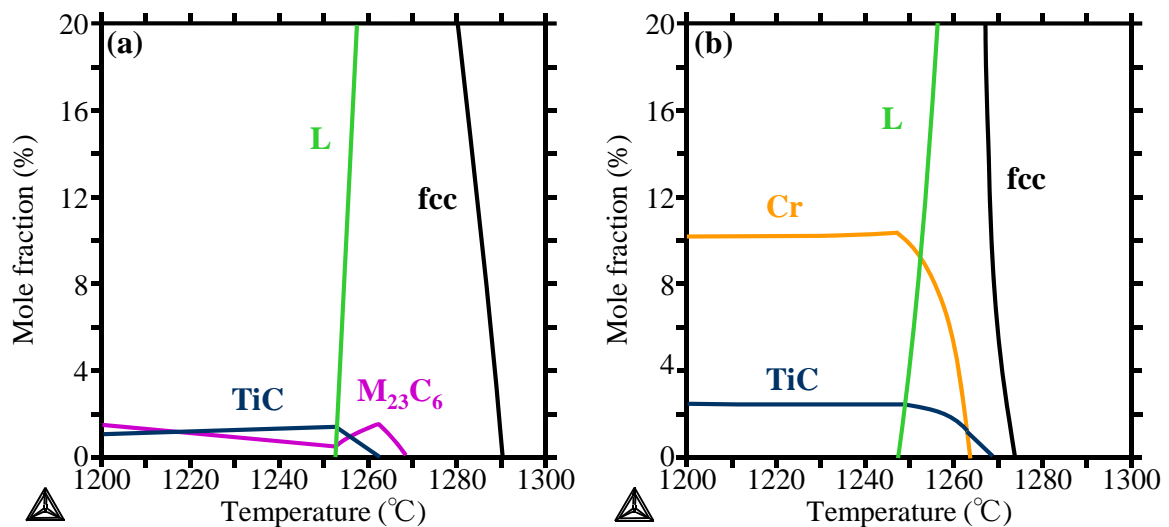


Fig. 8 Calculated phase equilibrium diagrams based on chemical compositions of liquid phase during final stages of solidification shown in Table 3 for (a) Ni₂M-stabilized alloy and (b) Alloy 690.

Although the results shown in Fig. 7 indicate that $M_{23}C_6$ is not predicted to form using the Scheil-Gulliver model with back diffusion of the C solute in the solid phase taken into consideration, there is still room for improvement of the simulations. For example, the effect of N on phase stability could be considered. Regardless, the present simulation results indicate that the Ni_2M -stabilized alloy is more likely to contain $M_{23}C_6$ than the Alloy 690, despite the fact that the C and Cr contents are the same, as shown in Table 1. Since $M_{23}C_6$ precipitates formed during the solidification process are expected to be much coarser than those formed during the TT process, it is considered that the coarse chromium carbide precipitates observed at grain boundaries in the Ni_2M -stabilized alloy shown in Fig. 3 are $M_{23}C_6$ carbides crystallized directly from the liquid and are not dissolved during the subsequent MA process. The existence of such residual coarse precipitates is not only likely to have a detrimental effect of the mechanical properties, but would also suppress the formation of fine coherent chromium carbide precipitates, which are considered to prevent intergranular fracture [19,20], during the TT process. In addition, the presence of $M_{23}C_6$ precipitates is expected to give rise to the presence of some smaller grains in the matrix due to grain-boundary pinning, which would lead to a duplex grain structure. This is supported by the fact that both the experimental and calculation results indicated no clear correlation between the presence of titanium carbonitride precipitates and the duplex grain structure, as shown in Figs. 3, 6 and 8. Since the presence of the coarse $M_{23}C_6$ precipitates may also increase the susceptibility of the material to SCC, methods for eliminating this need to be considered. This could be achieved either by reducing the initial C content, which would decrease the thermodynamic stability of $M_{23}C_6$, or by heavy forging before the MA process, which would promote dissolution of the coarse precipitates. Further investigation is required in order to clarify the effect of the duplex grain structure on the SCC susceptibility, and this will be carried out in the near future.

4. Conclusion

Grain boundaries in Ni_2M -stabilized alloy and Alloy 690 with and without a duplex grain structure, respectively, were experimentally characterized in order to determine the relationship between grain-boundary precipitates and the grain structure. Thermodynamic calculations based on the Scheil-Gulliver model were also performed in order to clarify the solidification process for the two alloys. The main conclusions of the present study are as follows.

- (1) FE-AES elemental mapping indicated that chromium carbide precipitates, which are predicted to be $M_{23}C_6$, are present in both alloys, but are considerably coarser in the Ni_2M -stabilized alloy.
- (2) Although Fe, Ti and B show no tendency to segregate at grain boundaries, P segregation does occur. For both alloys, only a few coarse titanium carbonitride precipitates are observed on the fracture surfaces, and all the analyzed elements exhibit a uniform distribution on intragranular fracture surfaces, which indicates that no localization occurs inside grains.
- (3) Simulation of the solidification process predicts that $M_{23}C_6$ is likely to be crystallized from the liquid during the final stages of solidification, and this occurs more readily in the Ni_2M -stabilized alloy.
- (4) The duplex grain structure in the Ni_2M -stabilized alloy is likely to be caused by the coarse $M_{23}C_6$ precipitates, which suppress the growth of some grains. Such precipitates are not only likely to degrade the mechanical properties but may also increase the susceptibility of the material to SCC.

Acknowledgement

The authors are indebted to professor Qunjia J. Peng, Institute of Metal Research, Chinese Academy of Sciences, for his assistance in the FE-AES analyses and other experimental techniques.

References

- [1] Y. Masuko: "Studies on Duplex-Grain Structures of Austenite (I) – Effect of Duplex-Grain Structures on Properties of Steel (Part-1)", *Tetsu-to-Hagane*, Vol.43, No.12, pp.1307-1312 (1957) (in Japanese).
- [2] Y. Masuko: "Studies on Duplex-Grain Structures of Austenite (I) – Effect of Duplex-Grain Structures on Properties of Steel (Part-2)", *Tetsu-to-Hagane*, Vol.44, No.1, pp.28-32 (1958) (in Japanese).

- [3] Y. Masuko: "Studies on Duplex-Grain Structures of Austenite (II) – Causes of Formation of Duplex-Grain Structures in Steels (Part-1)", *Tetsu-to-Hagane*, Vol.44, No.4, pp.476-479 (1958) (in Japanese).
- [4] Y. Masuko: "Studies on Duplex-Grain Structures of Austenite (II) – Causes of Formation of Duplex-Grain Structures in Steels (Part-2)", *Tetsu-to-Hagane*, Vol.44, No.5, pp.559-564 (1958) (in Japanese).
- [5] W. J. Mills and C. M. Brown: "Fracture Toughness of Alloy 600 and an EN82H Weld in Air and Water", *Metallurgical and Materials Transactions A*, Vol.32A, No.5, pp.1161-1174 (2001).
- [6] B. Z. Hyatt and C. M. Brown: "Microstructure and Mechanical Properties of Stress Relieved Electron Beam Welded Alloy 625", *Proceedings of 5th International Special Emphasis Symposium on Superalloys 718, 625, 706 and Various Derivatives*, TMS, Pennsylvania, USA, June 17-20, pp.645-656 (2001).
- [7] R. R. Shen: "Review of the Effect of Cold Work on Stress Corrosion Cracking of Alloy 690", *Postgraduate Seminar on Engineering Materials*, Espoo, Finland, September 5-6, pp.133-145 (2012).
- [8] P. L. Andresen, M. M. Morra, A. Ahluwalia, and J. Wilson: "SCC of Alloy 690 in high temperature water", *Proceedings of NACE Annual Corrosion Conference & Expo*, Texas, USA, March 14-18, paper 10241 (2010).
- [9] D. R. Tice, S. L. Medway, N. Platts, and J. W. Stairmand: "Crack growth testing on cold worked Alloy 690 in primary water environment", *Proceedings of 15th International Conference on Environmental Degradation of Materials in Nuclear Power Systems*, ANS, Colorado, USA, August 7-11, pp.71-87 (2011).
- [10] T. Horiuchi, K. Kuwano and N. Satoh: "Effect of Alloying Elements on the Stability of Ni₂M in Alloy 690 Based upon Thermodynamic Calculation", *Corrosion Engineering*, Vol.61, No.3, pp.74-78 (2012).
- [11] N. Satoh and T. Horiuchi: "Microstructure Evolution of Ni₂M-stabilized Alloy during Isothermal Heat Treatment", *Corrosion Engineering*, Vol.62, No.2, pp.58-61 (2013).
- [12] G. H. Gulliver: "The quantitative effect of rapid cooling upon the constitution of binary alloys", *Journal of the Institute of Metals*, Vol.9, pp.120-157 (1913).
- [13] E. Scheil: "Bemerkungen zur Schichtkristallbildung", *Zeitschrift für Metallkunde*, Vol.34, pp.70-72 (1942).
- [14] INCONEL: "Alloy 690", No.SMC-079, Special Metals Corporation, October (2009).
- [15] C. Beckermann: "Macroseggregation", *Casting*, ASM Handbook, Vol.15, ASM International, pp.348-352 (2008).
- [16] D.R. Poirier and J.C. Heinrich: "Modeling of Microseggregation and Macroseggregation", *Casting*, ASM Handbook, Vol.15, ASM International, pp.445-448 (2008).
- [17] J.-O. Andersson, T. Helander, L. Hoglund, P. Shi and B. Sundman: "Thermo-Calc & DICTRA, computational tools for materials science", *Calphad*, Vol.26, Issue 2, pp.273-312 (2002).
- [18] N. Saunders: "Phase Diagram Calculations for Ni-based Superalloys", *Proceedings of 8th International Symposium on Superalloys*, TMS, Pennsylvania, USA, September 22-26, pp.101-110 (1996).
- [19] J. M. Sarver, J. R. Crum and W. L. Mankins: "Carbide precipitation and the effect of thermal treatments on the SCC behavior of INCONEL Alloy 690", *Proceedings of 3rd International Symposium on Environmental Degradation of Materials in Nuclear Power Systems*, ANS, Traverse, USA, August 30-September 3, pp.581-586 (1987).
- [20] J. M. Sarver, J. V. Monter and B. P. Miglin: "The effect of thermal treatments on the microstructure and SCC behavior of Alloy 690", *Proceedings of 4th International Symposium on Environmental Degradation of Materials in Nuclear Power Systems*, ANS, Jekyll, USA, August 6-10, pp.47-63 (1989).